Catalysis Science & Technology

PAPER

View Article Online
View Journal | View Issue

Cite this: *Catal. Sci. Technol.*, 2016, **6**, 4840

Shape dependence of nanoceria on complete catalytic oxidation of *o*-xylene†

Lian Wang,[a] Yafei Wang,[a] Yan Zhang,[a] Yunbo Yu,*[ab] Hong He,*[ab] Xiubo Qin[c] and Baoyi Wang[c]

Received 25th January 2016,
Accepted 21st February 2016

DOI: 10.1039/c6cy00180g

www.rsc.org/catalysis

BTX (benzene, toluene, and xylene) in atmosphere, mainly emitted from various industrial processes and transportation activities, are of particular concern due to their potentially highly toxic effects on human health. Catalytic oxidation of *o*-xylene was investigated on nanosized CeO_2 particles, cubes, and rods, among which rods show the highest activity, which is comparable with those of traditional noble-metal catalysts. CeO_2 nanorods also exhibit long durability for *o*-xylene oxidation, without deactivation during a 50 h time-on stream test. Over the CeO_2 rods and particles, the presence of water vapor slightly decreased *o*-xylene conversion, while water vapor enhanced *o*-xylene oxidation on the CeO_2 cubes. High-resolution transmission electron microscopy, X-ray photoelectron spectroscopy, positron annihilation spectroscopy, and O_2 temperature-programmed desorption measurements revealed that ceria rods enclosed by (111) and (100) facets exhibit the highest concentration of oxygen vacancy clusters (VCs), the presence of which promoted the adsorption of molecular oxygen. The lower the temperature for desorption of chemisorbed O_2 species is, the higher is the activity for *o*-xylene oxidation, identifying the key role of VCs in this reaction *via* the activation of molecular oxygen over nanoceria. The finding may also be fundamental for designing ceria-based catalysts with better performance for catalytic oxidation of volatile organic compounds.

Introduction

Volatile organic compounds (VOCs), mainly emitted from various industrial processes and transportation activities, are classified as hazardous air pollutants either because of their toxic nature and/or their being precursors of ozone and photochemical smog.[1–3] Among them, BTX (benzene, toluene, and xylene) have attracted much attention because of their highly toxic potential. To date, many techniques have been developed to remove BTX from polluted air, such as adsorption, thermal oxidation, photocatalytic oxidation and catalytic oxidation, among which catalytic oxidation is one of the most environmentally friendly techniques due to its easy application, high efficiency and low cost.[4–8] Over the past few decades, complete catalytic oxidation of BTX has been widely studied over either supported noble metal or metal oxide catalysts.[9–20] Generally, noble metal catalysts exhibit higher activity than other metal oxide catalysts, and the former are more expensive than the latter. Therefore, it would be highly desirable to create noble-metal-free catalysts with high activity.

Ceria (CeO_2) has been extensively investigated in heterogeneous catalytic reactions such as automotive exhaust purification, water-gas shift reactions, CO oxidation, and production and purification of hydrogen. This largely originates from the remarkable ability of ceria to store and release oxygen depending on the formation of oxygen vacancies.[21–24] More recently, CeO_2-based catalysts have also been employed in BTX removal.[13–18,25,26] A variety of metal oxides (M_xO_y, M = Al, Ce, Mg, Mn, La, Ti) was used as supports for preparation of Pt catalysts, among which Pt/CeO_2 was the most active for toluene oxidation, due to its superior reducibility.[25] Luo *et al.*[13] reported that CeO_2–Y_2O_3 supported Pd catalysts were active for catalytic combustion of toluene with long-term stability due to their excellent redox properties and the high stability of PdO species. Mn–Ce/γ-Al_2O_3 catalysts were also developed for catalytic oxidation of toluene, in which cerium

[a] *State Key Joint Laboratory of Environment Simulation and Pollution Control, Research Center for Eco-Environmental Sciences, Chinese Academy of Sciences, Beijing, 100085, China. E-mail: ybyu@rcees.ac.cn, honghe@rcees.ac.cn*
[b] *CAS Center for Excellence in Urban Atmospheric Environment, Chinese Academy of Sciences, Xiamen 361021, China*
[c] *Key Laboratory of Nuclear Analysis Techniques, Institute of High Energy Physics, Chinese Academy of Sciences, Beijing 100049, China*

† Electronic supplementary information (ESI) available: Experimental details of EPR, comparison between the catalytic activity of nanoceria for *o*-xylene oxidation and those of different catalysts previously reported, XRD patterns, physicochemical properties of CeO_2 nanomaterials, Raman spectra, PAS spectra, XPS binding energies of individual peaks of the Ce 3d and Ce^{3+} concentration, integrated areas of O_2-TPD over nanoceria, and lattice strain of different crystal facets of nanoceria. See DOI: 10.1039/c6cy00180g

improves the catalytic role of manganese in toluene oxidation.[17] More recently, pure CeO_2–MnO_x composite oxides prepared using a hydrothermal method were employed in catalytic removal of benzene, during which MnO_x provided available oxygen species and the presence of CeO_2 enhanced oxygen mobility. Such a synergistic effect was determined for benzene oxidation with high efficiency.[18]

Over the past few decades, extensive studies have demonstrated that the size and shape of a catalyst particle on the nanometre scale profoundly affect its catalytic performance.[27] Achievements in morphology-controlled synthesis of nanostructured materials have been presenting exciting opportunities for creating catalyst particles that are all of the same size and shape.[28] Keeping this in mind, CeO_2 nanoparticles, nanorods and nanocubes with well-defined reactive crystal planes have been synthesized, providing an opportunity to design catalysts with desired performance.[27,29] Our previous study showed that CeO_2 nanocubes prepared using a facile hydrothermal method exhibit high activity for complete catalytic oxidation of *o*-xylene at low temperatures.[30] Since water vapor is typically present in various exhausts, it is thus of importance to develop catalysts that are active in the presence of water vapor. Unfortunately, little information can be obtained involving BTX removal over well-defined CeO_2 nanomaterials, particularly in the presence of water vapor.

Herein, CeO_2 nanorods, nanocubes and nanoparticles were synthesized and employed in catalytic oxidation of *o*-xylene. It is interesting that the CeO_2 nanorods exhibit higher activity for *o*-xylene oxidation, originating from the higher concentration of oxygen vacancy clusters in the nanorods than those in the nanoparticles and nanocubes. Also, it was firstly found that the influence of water vapor on *o*-xylene oxidation was closely related to the morphology of nanoceria.

Experimental

Catalyst preparation

CeO_2 nanocubes and nanorods were synthesized using a solution-based hydrothermal method, as was reported previously.[31,32] Specifically, 3.0 g of $Ce(NO_3)_3{\cdot}6H_2O$ (AR grade, Sinopharm Chemical Reagent Co., Ltd., China) was dissolved in deionized water and mixed with 21 ml of NaOH solution with a specific concentration (1 mol L^{-1} for cubes, while 10 mol L^{-1} for rods) in a 100 ml Teflon-lined bottle. After stirring for 15 min, the mixture was hydrothermally treated at 100 °C for 12 h in a stainless steel autoclave. After that, fresh white precipitates were separated by centrifugation, washed with deionized water thoroughly to remove any possible ionic remnants, and dried at 60 °C in air for 24 h and calcined at 450 °C for 4 h. CeO_2 nanoparticles were prepared using a traditional precipitation method: $Ce(NO_3)_3{\cdot}6H_2O$ was dissolved in deionized water, and then appropriate amounts of 1 mol L^{-1} NaOH solution were rapidly added with stirring. After aging for 24 h, the precipitate was centrifuged, and further procedures used were similar to those employed in the preparation of CeO_2 nanocubes and nanorods.

Catalytic activity test

Catalytic activity tests were carried out in a continuous flow fixed-bed quartz reactor (i.d. = 5 mm), containing 0.1 g of catalyst samples (40–60 mesh). Before the measurement, the sample was pretreated in 20 vol% O_2/N_2 for 30 min at 300 °C. A gas mixture containing 250 ppm *o*-xylene (150 ppm for durability and water vapor influence tests), and 20% O_2 in N_2 was fed at a total flow rate of 100 ml min^{-1}, with a weight hourly space velocity (WHSV) of 60 000 ml h^{-1} g^{-1}. The components of the outlet gas stream were analyzed on-line using a GC-MS (Agilent 6890-5973N, HP 5MS) and a GC equipped with a FID (Shangfen GC-112A, TDX-01 column). The conversion of *o*-xylene was calculated using the following equation:

$$o\text{-Xylene conversion}\,(\%) = \frac{C_{o\text{-xylene (in)}} - C_{o\text{-xylene (out)}}}{C_{o\text{-xylene (in)}}} \times 100\%$$

where $C_{o\text{-xylene (in)}}$ (ppm) and $C_{o\text{-xylene (out)}}$ (ppm) are the concentrations of *o*-xylene in the inlet and outlet gas streams, respectively.

Catalyst characterization

The BET surface areas of CeO_2 were determined on a Quantasorb-18 automatic instrument by physical adsorption measurements with N_2 at −196 °C, before which the samples were degassed at 300 °C for 4 h. Powder X-ray diffraction (XRD) patterns were measured on a PANalytical X'Pert PRO X-ray diffractometer (Japan, CuK_α as the radiation source, λ = 0.154 nm). TEM images were obtained on a Hitachi H-7500 transmission electron microscope with an acceleration voltage of 80 kV. HRTEM images were measured on a JEOL JEM 2011 TEM with an acceleration voltage of 200 kV.

Raman spectra were obtained at room temperature using a UV resonance Raman spectrometer (UVR DLPC-DL-03) equipped with a CCD detector cooled by liquid N_2. The instrument was calibrated against the Stokes Raman signal of Teflon at 1378 cm^{-1}. A continuous diode pumped solid state (DPSS) laser beam (532 nm) was used as the exciting radiation, and a 40 mW power source was used. The spectra resolution reported here was 2.0 cm^{-1}.

XPS spectra were carefully recorded in a scanning X-ray microprobe (PHI Quantera, ULVAC–PHI, Inc) using AlK_α radiation with a step size of 0.1 eV. The base pressure during the analysis was 10^{-9} Torr. Before measurement, all the samples were vacuumed in an XPS chamber for 30 min. The binding energies of Ce 3d and O 1s were calibrated using C 1s (BE = 284.8 eV) as the standard. The experimental spectra of Ce 3d and O 1s were approximated by using a Gaussian curve.

PAS measurements were conducted with a magnetically guided variable-energy (0–20 keV) positron beam. Doppler broadening of positron annihilation radiation is characterized by *S* and *W* parameters. *S* is defined as the ratio of the

g-ray counts in the central part of the 511 keV peak (510.24–511.76 keV) to that in the entire peak (504.2–517.8 keV). The *W* parameter is defined as the ratio of the summed g-ray counts in the ranges of 513.6–517.8 keV and 504.2–508.4 keV to the total number of counts in the entire peak. The positron annihilation results were analyzed with the POSITRONFIT-88 program.

Oxygen temperature-programmed desorption (O_2-TPD) experiments were conducted over 100 mg of samples, and the O_2 signal (m/z = 32) was monitored online using a quadrupole mass spectrometer (HPR20, Hiden Analytical Ltd.). Before the measurement, the samples were pretreated in a flow of N_2 (30 ml min^{-1}) at 300 °C for 60 min and cooled down to room temperature. After O_2 adsorption for 60 min (30 ml min^{-1}), the feed gas was switched to He to purge the system (for 30 min) and then the temperature was raised to 800 °C at a ramp of 10 °C min^{-1} in a stream of He at 30 ml min^{-1} and the mass signal of O_2 (m/z = 32) was recorded simultaneously.

Electron spin resonance (EPR) spectra in the X-band were recorded at −196 °C using a JES-FA200 (JEOL) CW spectrometer at a microwave power of 1 MW, a modulation frequency of 100 kHz and central field of 325 mT. Before the measurement, the samples (100 mg) were pretreated in a flow of N_2 at 300 °C for 1 h, and the detailed information is presented in the ESI.†

Results and discussion

Catalytic activity of nanoceria for *o*-xylene oxidation

The catalytic activities of the CeO_2 nanomaterials with different shapes were investigated by *o*-xylene oxidation at different temperatures, during which a clear shape dependence was observed (Fig. 1 and Table 1). Over the nanoparticles, oxidation of *o*-xylene was hardly detected at a temperature of 195 °C. When temperature was increased, catalytic oxidation was triggered significantly, exhibiting 50% *o*-xylene conversion (T_{50}) at 219 °C. Further increasing the reaction temperature resulted in a gradual increase in *o*-xylene conversion, during which 90% conversion (T_{90}) and complete oxidation were achieved at 272 and 300 °C, respectively. In the complete oxidation of *o*-xylene, meanwhile, GC-MS results showed that CO_2 and H_2O were the only detectable products. Compared with the nanoparticles, a similar value of T_{50} for *o*-xylene oxidation was observed over the nanocubes, while the samples exhibited higher activity at temperatures below 210 °C and within a temperature range of 220–280 °C. The nanorods showed the highest activity for *o*-xylene oxidation particularly at low temperatures, exhibiting T_{50} at 195 °C. Over the nanorods, it should be noted that the specific rate at 210 °C was up to 1.48 × 10^{-3} μmol s^{-1} m^{-2}, which is 1.8 times greater than that of the nanoparticles. Obviously, the CeO_2 nanomaterials exhibit high activity for *o*-xylene oxidation which is similar to those of noble metal catalysts (supported Pt and Pd catalysts), while much higher than those of noble-metal-free catalysts reported elsewhere (Table S1†).[33–39]

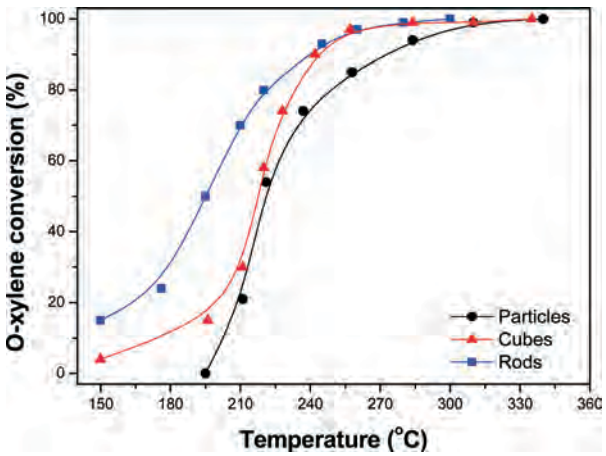

Fig. 1 Activity of CeO_2 nanomaterials with different shapes for *o*-xylene oxidation. Reaction conditions: catalyst weight 0.1 g, *o*-xylene 250 ppm, 20 v/v% O_2, N_2 balance, total flow rate = 100 ml min^{-1}, WHSV = 60 000 ml h^{-1} g^{-1}.

The durability of the CeO_2 rods for *o*-xylene oxidation was also evaluated at 220 °C, and the results are shown in Fig. 2. Throughout the operation time of 50 h, obviously, *o*-xylene conversion was always retained at 85%, indicating excellent durability for catalytic oxidation of *o*-xylene. The influence of water vapor on the activity of nanosized CeO_2 for *o*-xylene oxidation was measured at 220 °C (Fig. 3). Over the CeO_2 rods, *o*-xylene conversion was retained at 85% in the absence of water vapor. Introduction of 2% water vapor to the feed gas resulted in a gradual decrease in *o*-xylene conversion, which was retained at around 80% after 1 h. When water vapor was removed from the feed gas, the conversion of *o*-xylene recovered to its initial level as that in the absence of water vapor. This result indicates that the nanorods show high tolerance against water vapor for *o*-xylene oxidation, and the effect of water vapor was reversible. Slight temporary suppression of water vapor on *o*-xylene oxidation was also observed over the nanoparticles, which is 4% lower than that in the absence of water vapor. Over the CeO_2 cubes, however, water vapor enhanced *o*-xylene oxidation, exhibiting an increase of around 4% in *o*-xylene oxidation if 2 vol% water vapor was introduced. Such an enhancement was further promoted by an increase in the concentration of water vapor to 5 vol%.

Structural features of nanoceria

XRD analysis (Fig. S1†) revealed that the prepared CeO_2 materials could be indexed to a pure fluorite cubic structure (JCPDS 34-0394). This structural feature was also confirmed by Raman characterization (Fig. S2†), in which a strong band at 454–460 cm^{-1} was attributed to the vibrational mode of the F_{2g} symmetry.[40,41] By using the Scherrer equation, the average particle size of nanoceria was calculated based on the peak due to the (111) plane, and the results are shown in Table 1. The nanorods show an average particle size of 11.6

Table 1 Physicochemical properties, *o*-xylene oxidation rates over CeO_2 nanomaterials with different shapes

Sample	BET ($m^2\ g^{-1}$)	Particle size[a] (nm)	T_{50}[b] (°C)	T_{90}[c] (°C)	Reaction rate[d] ($\times10^{-3}$ μmol $s^{-1}\ m^{-2}$)
Particles	75.0	12.8	219	272	0.52
Cubes	76.9	13.4	217	242	0.72
Rods	88.2	11.6	195	239	1.48

[a] Calculated using the Scherrer equation over the peak due to the (111) plane. [b] Reaction temperature for 50% conversion of *o*-xylene (T_{50}). [c] Reaction temperature for 90% conversion of *o*-xylene (T_{90}). [d] Measured at 210 °C.

nm, which is a little smaller than that of the nanoparticles and nanocubes. As a result, it is reasonable that the nanorods exhibit a slightly larger specific surface area than the other two (Table 1).

The TEM images show that the prepared CeO_2 particles exhibit an irregular shape, with an average size of about 8–13 nm (Fig. 4A and Table S2†). Fig. 5A gives the HRTEM image of representative particles, in which the lattice spacings were measured to be 0.31 and 0.27 nm, implying that the particles predominantly expose the (111) and (100) planes, respectively.[31] In agreement with previous studies,[31,41] the CeO_2 cubes with a size of around 8–20 nm (Fig. 4B and 5B) are only enclosed by the (100) planes. Based on the interplanar spacings, the (111) and (100) side planes of the rods can be identified (Fig. 5C and D).[42] This result reveals that the rods which are 40–300 nm in length and ~8–13 nm in diameter (Fig. 4C and Table S2†) predominantly expose the (111) and (100) planes.

Oxygen species and vacancies on the surface of nanoceria

The O 1s core level spectra of CeO_2 with different shapes are presented in Fig. 6A. The peak with a low binding energy (529.0–529.1 eV) is attributed to lattice oxygen of the crystalline network.[43] The high binding energy side at 531.3–532.0 eV corresponds to oxygen species located on the surface,[43] in which the binding energy drops in the sequence particles > cubes > rods.

XPS analysis was also performed to characterize the valence state of the Ce ions over nanoceria (Fig. 6B). The v_0, v', u_0, and u' peaks correspond to Ce^{3+}; while v, v'', v''', u, u'', u''' are attributed to Ce^{4+}.[43,44] The peak positions for all the samples are listed in Table S3.† The Ce^{3+} concentration in the CeO_2 nanomaterials was calculated by analysis of the integrated peak area (ESI†). In all the samples, the presence of Ce^{3+} was clearly identified by XPS analysis, with concentrations in the range of 21.1–24.4% (Table S3†), which was in good agreement with previous results.[43,44] These results indicate that oxygen vacancies are generated to maintain the electrostatic balance of Ce^{3+}-containing fluorite ceria.[45] Based on the relative concentration of Ce^{3+}, it is shown that the concentration of oxygen vacancies on the CeO_2 nanomaterials follows the order particles ≈ rods > cubes. Further evidence identifying the formation of oxygen vacancies was provided by Raman characterization (Fig. S2B†), in which a band at around 598 cm^{-1} was due to a defect-induced (D) mode of ceria.[40,41] By comparing the relative intensity of the peak due to the D mode with that of the F_{2g} mode,[41] we can roughly estimate that the concentration of the oxygen vacancies on the CeO_2 nanorods and nanoparticles was higher than that on the nanocubes, further confirming the result of Ce 3d XPS.

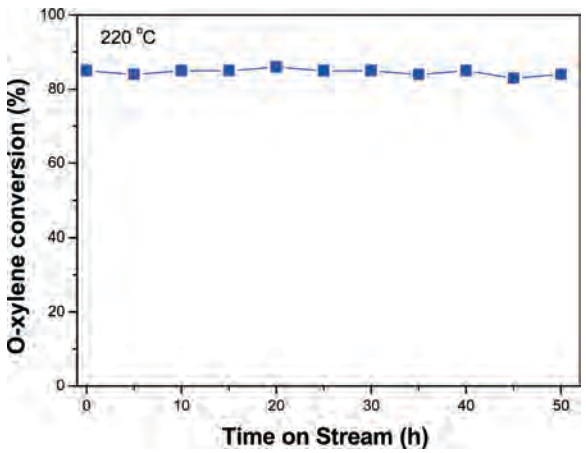

Fig. 2 Durability of CeO_2 rods for *o*-xylene oxidation at 220 °C. Reaction conditions: catalyst weight 0.1 g, *o*-xylene 150 ppm, 20 vol% O_2, N_2 balance, total flow rate = 100 ml min^{-1}, WHSV = 60 000 ml h^{-1} g^{-1}.

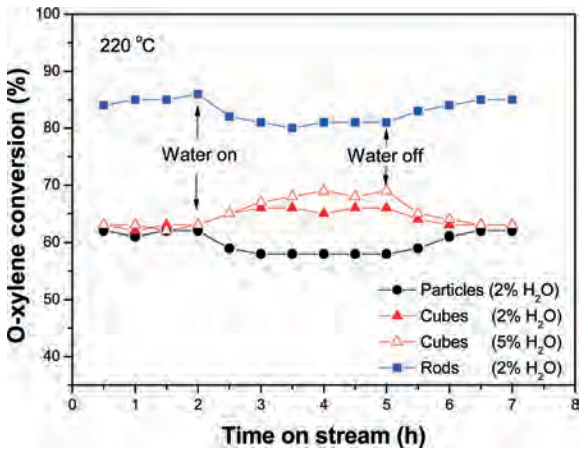

Fig. 3 Influence of water vapor on the activity of CeO_2 nanomaterials with different shapes for *o*-xylene oxidation at 220 °C. Reaction conditions: catalyst weight 0.1 g, *o*-xylene 150 ppm, 20 vol% O_2, 2 vol% (or 5 vol%) H_2O (if used), N_2 balance, total flow rate = 100 ml min^{-1}, WHSV = 60 000 ml h^{-1} g^{-1}.

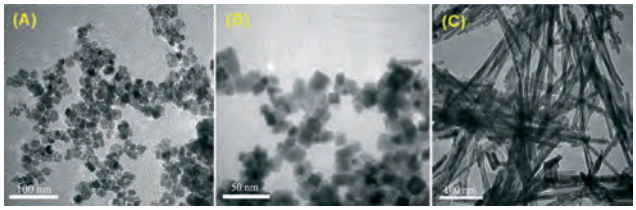

Fig. 4 TEM images of CeO_2 particles (A), cubes (B), and rods (C).

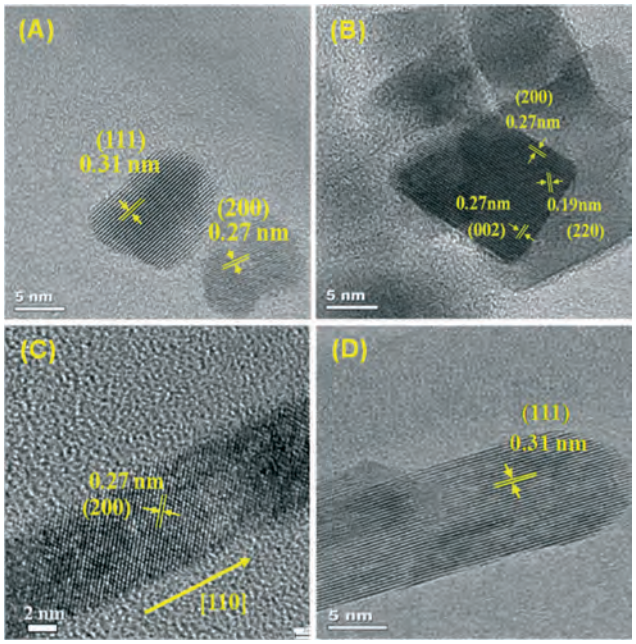

Fig. 5 HRTEM images of CeO_2 particles (A), cubes (B), and rods (C and D).

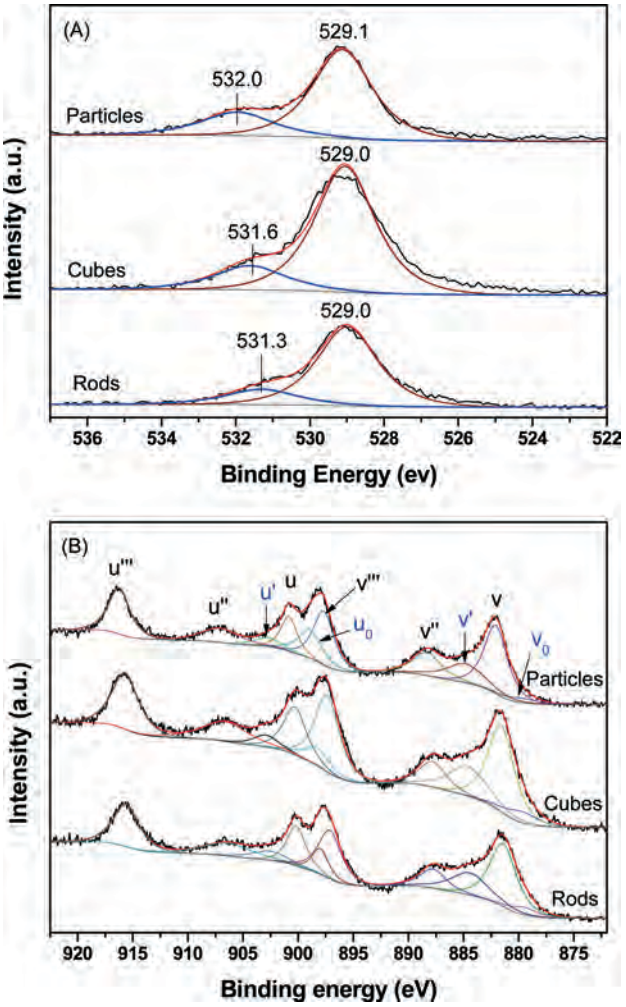

Fig. 6 O 1s (A) and Ce 3d (B) XPS spectra of CeO_2 with different shapes.

PAS characterization was further used to reveal the structural features of the oxygen vacancies in nanoceria (Fig. S3†). The lifetime of positrons is governed by the average electron density at an annihilation site, which increases with a decrease in the average electron density. With this in mind, one can easily distinguish the features of defects in solid materials, such as the size and intensity of defects.[46] In agreement with previous studies,[42,47–49] the lifetimes of all the samples exhibit three distinct components, τ_1, τ_2, and τ_3, together with corresponding intensities denoted as I_1, I_2, and I_3 (Table 2). The longest component, τ_3, with the lowest intensity, was generally due to the annihilation of ortho-positronium atoms in the large voids present in the sample. In previous studies,[42,47–49] the shortest one (τ_1) within a wide range of 172–247 ps, was observed over nanoceria, attributed to free annihilation of positrons ($\tau_1 \sim$ 172–187 ps) or annihilation of positrons in small oxygen vacancies, such as single oxygen vacancies in CeO_2 ($\tau_1 \sim$ 188–247 ps). In our case, the values of τ_1 were 181 ps for cubes, 183 ps for rods, and 202 ps for particles. As a result, the τ_1 components of the CeO_2 cubes and rods can be related to free annihilation of positrons, while this component of particles may arise from annihilation of positrons in mono-oxygen vacancies. The middle one (τ_2) is often assigned to oxygen vacancy clusters (denoted as VCs hereafter, *i.e.* dimers, trimers, or larger), resulting from aggregation of single oxygen vacancies. Among all the samples, it is interesting to note that the cubes exhibited the smallest τ_2 value (340 ps) with the lowest relative concentration (57.1%). Over the rods, the second-largest τ_2 value (407 ps) was observed with the highest intensity of 62.4%. These results clearly show that the size and concentration of VCs are strongly dependent on the morphology of CeO_2.

It is widely accepted that oxygen vacancies dominate the electronic and chemical properties of ceria, thus providing abundant active sites for the adsorption of molecular oxygen.[45] To highlight this issue, O_2-TPD experiments were

Table 2 Position lifetime parameters of CeO_2 nanomaterials

Sample	τ_1 (ps)	τ_2 (ps)	τ_3 (ns)	I_1 (%)	I_2 (%)	I_3 (%)
Particles	202	450	2.72	40.2	58.5	1.3
Cubes	181	340	2.79	41.5	57.1	1.4
Rods	183	407	2.77	36.1	62.4	1.5

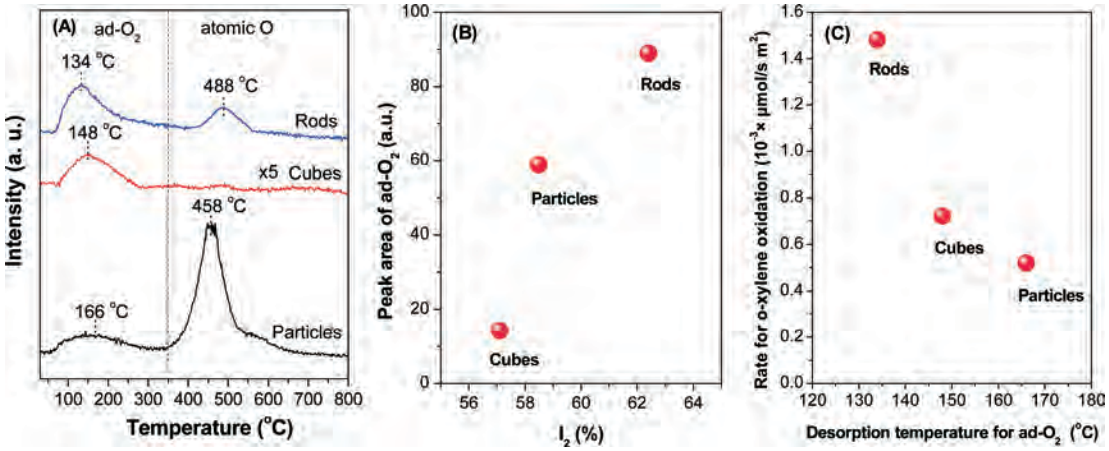

Fig. 7 (A) O_2-TPD curves of CeO_2 nanomaterials; (B) relationship between the peak area of adsorbed molecular oxygen (ad-O_2) and the relative intensity of oxygen vacancy clusters (I_2) in CeO_2 nanomaterials; (C) relationship between the desorption temperature for ad-O_2 and the reaction rate for *o*-xylene oxidation over CeO_2 nanomaterials.

performed over CeO_2 with different shapes after pretreatment in N_2 at 300 °C and subsequent O_2 adsorption at 30 °C (Fig. 7A and Table S4†). Over the CeO_2 nanoparticles, a strong O_2 desorption peak centered at 458 °C was observed, which was accompanied by a weak peak located at 166 °C. The low temperature peak was assigned to desorption of molecular oxygen, while the high temperature one was attributed to the desorption of atomic oxygen species on the surface of CeO_2.[21,22,41,50] Two peaks due to O_2 desorption were also observed on the CeO_2 nanorods; the low-temperature one exhibits a much stronger intensity centered at 32 °C which is lower than that of the nanoparticles. In the O_2-TPD experiments over CeO_2 nanocubes, however, only one peak centered at 148 °C was observed.

Relationship between structure of ceria and activity for *o*-xylene oxidation

As is shown in Fig. 1 and Table 1, the CeO_2 nanorods exhibit much higher low-temperature activity for *o*-xylene oxidation than nanocubes and nanoparticles. Generally, nanocatalytic materials with high surface area possess numerous crystal faces, edges, and corners, the presence of which have been considered to provide abundant active sites for the adsorption and activation of reductants, thus exhibiting better catalytic activity. In the present study, however, the nanosized CeO_2 particles, cubes, and rods exhibit a similar average particle size and similar specific surface area, which cannot account for their different behaviors in *o*-xylene oxidation. This situation was further confirmed by the specific reaction rate normalized by the surface area (Table 1).

Recent advances in nanomaterial synthesis and characterization also clearly identified that the catalytic behavior of nanoceria was strongly dependent on its surface structure. By using a solution-based hydrothermal method, CeO_2 nanorods exposing reactive (110) and (100) facets were created, exhibiting much higher activity for CO oxidation than nanoparticles enclosed by the stable (111) planes and nanocubes enclosed by the (100) planes.[32,47] As was revealed by Wu *et al.*,[51] the turnover frequency of CO oxidation on the planes of the CeO_2 nanocrystals drops in the sequence (110) > (100) > (111), which is in agreement with the theoretical prediction and the experimental results.[52–55] Specifically, the ease of oxygen extraction from the surface plane of ceria is directly related to its catalytic reactivity, which in turn reveals the crucial role of oxygen vacancies on ceria surfaces in the adsorption and activation of O_2, thus related to CO oxidation.

Mitsui *et al.*[56] reported that even for the simple reaction of H_2 dissociation on a model Pd(111) catalyst, aggregates of three or more hydrogen vacancies are required, indicating the crucial role of vacancy clusters in catalytic reactions. Similarly, the calculated results provided by Jiang *et al.*[57] also revealed that two neighboring single oxygen vacancies working together are more efficient for O_2 activation than those working alone, and thus VCs contribute to CO oxidation on the Co_3O_4(110) surface. Recently, Liu *et al.*[42] further identified that the concentration of oxygen vacancy clusters on CeO_2 nanorods enclosed by (111) and (100) facets was much higher than that on CeO_2 nanorods enclosed by (110) and (100) facets. Such intrinsic properties in VCs guarantee a higher activity of the former for CO oxidation. By low pressure thermal activation, CeO_2 nanorods and nanoparticles enriched with oxygen vacancies have been created, exhibiting high activity for CO oxidation.[44] With these in mind, Fig. 7B presents the relationship between the peak area for chemisorbed O_2 (Table S4†) and the relative intensity of VCs (I_2) in CeO_2 with different shapes. Clearly, a higher concentration of VCs results in a larger amount of adsorbed O_2, strongly suggesting the key roles of VCs in the adsorption and activation of O_2. More recently, a monotonous increase in O_2 adsorption with increasing VCs on Co_3O_4 was also observed in our previous studies, the presence of which guarantees the high activity of Co_3O_4 for CO oxidation at low temperatures.[58,59]

By using Raman and TPD measurements, the role of oxygen vacancies in adsorption of O_2 was carefully analysed.[40,41] Over reduced nanoceria (pretreated by H_2 and CO), it was

found that the single oxygen vacancies and their aggregates serve as efficient traps for adsorption and activation of O_2, which are present as superoxide (O_2^-) and peroxide (O_2^{2-}) species by electron extraction from the Ce^{3+} ions on the oxygen vacancies. The relationship between single oxygen vacancies and the formation of O_2^- and O_2^{2-} on the CeO_2 surface was further confirmed by DFT+U calculations.[50] In our case, ESR measurements (Fig. S4†) confirm the formation of O_2^- during exposure of CeO_2 to O_2, giving the *g* values of 2.003–2.034.[43] It is interesting to note that the lower the temperature for desorption of chemisorbed O_2 species is, the higher is the activity for *o*-xylene oxidation (Fig. 7C), identifying the key role of VCs in this reaction *via* the activation of molecular oxygen.

If one considers that the CeO_2 cubes only contain reactive (100) facets, the question why their Ce^{3+} concentration is lower than those of rods and particles (Table S2†) may arise (both of which are enclosed by reactive (100) and inner (111) planes). A picture of hexagonal prism shaped ceria nanorods on an atomic level achieved by molecular dynamics simulation may provide a clue for getting the answer: the (100) surfaces have, in part, faceted into (111), presenting a sawtooth-like appearance and far from the perfect and ideal ones.[60,61] As a result, a variety of defects (kinks, steps, dislocations, vacancies, *etc.*) would be present on the surface of nanoceria, resulting in a microstrain of the ceria lattice. On these rough surfaces, meanwhile, low-coordinated O atoms are rich, the depletion of which is strongly facilitated compared to regular (100) and (111) plateaus, favoring the formation of oxygen vacancies in ceria.[61–63] With this in mind, we further analyzed the lattice strain of nanoceria, which was estimated using the single-line method from analysis of XRD line broadening using a pseudo-Voigt profile function.[64,65] Table S5† shows that the rods and particles exhibit much higher lattice strains than the cubes, which is in agreement with the results of Si and Flytzani-Stephanopoulos.[65] Taking the results presented in Table 2 and S3† into account, therefore, the lattice strain correlates with the formation of oxygen vacancies, and also is related to the concentration of Ce^{3+} in nanoceria with different shapes.

By optimization of synthesis conditions, Ce^{3+}–O–Ce^{4+}-type defect sites were created in nanoceria, promoting the oxidative dehydrogenation of ethylbenzene in the presence of N_2O.[66] Also, it has been reported that oxygen vacancies over nanocrystalline ceria play a crucial role in total oxidation of naphthalene.[67] As was reported by Wang *et al.*,[18] oxygen vacancies contributed to catalytic removal of benzene over CeO_2–MnO_x composite oxides. Our results presented here confirm that oxygen vacancy clusters, not single oxygen vacancies, are active sites for *o*-xylene oxidation *via* the activation of molecular oxygen. Our results may also be fundamental for creating ceria based catalysts with better performance for catalytic oxidation of VOCs.

Water adsorption is ubiquitous in oxide surfaces, as water may act as a promoter or as an inhibitor in a given reaction occurring over oxide surfaces. Numerous studies have been performed on the behaviors of water adsorption on ceria, particularly on the redox properties of ceria changed by water–ceria interactions.[45] Over regular (111), (100), and (110) CeO_2 surfaces, DFT+U calculations predicted that oxygen vacancies (single oxygen vacancies) are active sites for the associative and dissociative adsorption of water. As a result, water molecules strongly and dissociatively bind with oxygen vacancies, promoting further reduction of ceria.[68,69] With this in mind, one can easily deduce that the presence of water should promote the oxidation of *o*-xylene since oxygen vacancies play a crucial role in this reaction. In contrast to what has been found in the calculations, previous reduction/reoxidation cyclic experiments performed by Padeste *et al.* indicated that water will reoxidize reduced ceria with evolution of hydrogen, resulting in a transformation of surface Ce^{3+} into Ce^{4+}.[70] This result means that a decrease in the concentration of oxygen vacancies would occur during exposure of ceria to water, possibly lowering the *o*-xylene conversion with water present. As is shown in Fig. 3, water vapor enhances the activity of the CeO_2 cubes for *o*-xylene oxidation, and decreases the activity of the rods and particles. To reveal such a shape dependent influence of water vapor on the activity of ceria, further studies should be done. For example, is there something different between water adsorption on single oxygen vacancies and their aggregates? The detailed mechanism of catalytic oxidation of *o*-xylene over nanosized ceria should be understood.

Conclusions

Nanosized CeO_2 particles, cubes, and rods are highly active for catalytic oxidation of *o*-xylene, and are comparable with traditional noble-metal catalysts. The CeO_2 cubes only contain reactive (100) facets, while their activity for *o*-xylene oxidation is much lower than those of the rods and particles (both of which are enclosed by reactive (100) and inner (111) planes). XPS, Raman, PAS, and O_2-TPD measurements confirm the presence of oxygen vacancy clusters in the nanosized ceria, giving an opportunity for adsorption and activation of molecular oxygen. Among the three samples, the CeO_2 nanorods exhibit the highest concentration of VCs, on which the largest amount of O_2 was adsorbed; over this sample, meanwhile, the desorption of adsorbed O_2 species occurred at the lowest temperature. As a result, it is reasonable that the CeO_2 nanorods exhibit the highest activity for catalytic oxidation of *o*-xylene, clearly identifying the key role of VCs in this reaction *via* the activation of molecular oxygen over nanoceria. Moreover, a shape dependent influence of water vapor on the activity of ceria was firstly observed.

Acknowledgements

This work was financially supported by the National Natural Science Foundation of China (21373261 and 51278486) and the National High Technology Research and Development Program of China (863 Program, 2013AA065301).

Notes and references

1 B. J. Finlayson-Pitts and J. N. Pitts, Jr., *Science*, 1997, **276**, 1045–1051.
2 R. E. Dodson, E. A. Houseman, J. I. Levy, J. D. Spengler, J. P. Shine and D. H. Bennett, *Environ. Sci. Technol.*, 2007, **41**, 8498–8505.
3 R. H. Wang and J. H. Li, *Environ. Sci. Technol.*, 2010, **44**, 4282–4287.
4 J. Peral and D. F. Ollis, *J. Catal.*, 1991, **136**, 554–565.
5 F. I. Khan and A. K, Ghoshal, *J. Loss Prev. Process Ind.*, 2000, **13**, 527–545.
6 M. A. Hernández, J. A. Velasco, M. Asomoza, S. Solís, F. Rojas and V. H. Lara, *Ind. Eng. Chem. Res.*, 2004, **43**, 1779–1784.
7 L. F. Liotta, *Appl. Catal., B*, 2010, **100**, 403–412.
8 H. Huang, Y. Xu, Q. Feng and D. Y. C. Leung, *Catal. Sci. Technol.*, 2015, **5**, 2649–2669.
9 M. J. Patterson, D. E. Angove and N. W. Cant, *Appl. Catal., B*, 2000, **26**, 47–57.
10 C. Y. Chen, F. Chen, L. Zhang, S. X. Pan, C. Q. Bian, X. M. Zheng, X. J. Meng and F. S. Xiao, *Chem. Commun.*, 2015, **51**, 5936–5938.
11 S. Scir, S. Minic, C. Crisafulli, C. Satriano and A. Pistone, *Appl. Catal., B*, 2003, **40**, 43–49.
12 K. Okumura, T. Kobayashi, H. Tanaka and M. Niwa, *Appl. Catal., B*, 2003, **44**, 325–331.
13 M. F. Luo, M. He, Y. L. Xie, P. Fang and L. Y. Jin, *Appl. Catal., B*, 2007, **69**, 213–218.
14 C. H. Wang and S. S. Lin, *Appl. Catal., A*, 2004, **268**, 227–233.
15 M. Alifanti, M. Florea and V. I. Parvulescu, *Appl. Catal., B*, 2007, **70**, 400–405.
16 D. G. Angel, J. M. Padilla, I. Cuauhtemoc and J. Navarrete, *J. Mol. Catal. A: Chem.*, 2008, **281**, 173–178.
17 H.-J. Kim, S.-W. Choi and H. I. Inyang, *Environ. Technol.*, 2008, **29**, 559–569.
18 Z. Wang, G. L. Shen, J. Q. Li, H. D. Liu, Q. Wang and Y. F. Chen, *Appl. Catal., B*, 2013, **138–139**, 253–259.
19 Y. Wu, M. Liu, Z. Ma and S. Xing, *Catal. Today*, 2011, **175**, 196–201.
20 Y. Wu, Y. Lu, C. Song, Z. Ma, S. Xing and Y. Gao, *Catal. Today*, 2013, **201**, 32–39.
21 H. C. Yao and Y. F. Yu Yao, *J. Catal.*, 1984, **86**, 254–265.
22 A. Trovarelli, *Catal. Rev.: Sci. Eng.*, 1996, **38**, 439–520.
23 Q. Fu, H. Saltsburg and M. Flytzani-Stephanopoulos, *Science*, 2003, **301**, 935–938.
24 G. A. Deluga, J. R. Salge, L. D. Schmidt and X. E. Verykios, *Science*, 2004, **303**, 993–997.
25 S. M. Saqer, D. I. Kondarides and X. E. Verykios, *Top. Catal.*, 2009, **52**, 517–527.
26 L. F. Liotta, H. J. Wu, G. Pantaleo and A. M. Venezia, *Catal. Sci. Technol.*, 2013, **3**, 3085–3102.
27 Y. Li and W. J. Shen, *Chem. Soc. Rev.*, 2014, **43**, 1543–1574.
28 C. Burda, X. Chen, R. Narayanan and M. A. El-Sayed, *Chem. Rev.*, 2005, **105**, 1025–1102.
29 C. W. Sun, H. Li and L. Q. Chen, *Energy Environ. Sci.*, 2012, **5**, 8475–8505.
30 L. He, Y. B. Yu, C. B. Zhang and H. He, *J. Environ. Sci.*, 2011, **23**, 160–165.
31 H. X. Mai, L. D. Sun, Y. W. Zhang, R. Si, W. Feng, H. P. Zhang, H. C. Liu and C. H. Yan, *J. Phys. Chem. B*, 2005, **109**, 24380–24385.
32 K. B. Zhou, X. Wang, X. M. Sun, Q. Peng and Y. D. Li, *J. Catal.*, 2005, **229**, 206–212.
33 S. Y. Huang, C. B. Zhang and H. He, *J. Environ. Sci.*, 2009, **21**, 985–990.
34 S. C. Kim and W. G. Shim, *Appl. Catal., B*, 2009, **92**, 429–436.
35 Y. F. Wang, C. B. Zhang, F. D. Liu and H. He, *Appl. Catal., B*, 2013, **142–143**, 72–79.
36 P. H. Dégé, L. Pinard and P. Magnoux, *Appl. Catal., B*, 2000, **27**, 17–26.
37 M. N. Padilla-Serrano, F. J. Maldonado-Hódar and C. Moreno-Castilla, *Appl. Catal., B*, 2005, **61**, 253–258.
38 S. C. Kim, *J. Hazard. Mater.*, 2002, **91**, 285–299.
39 R. Beauchet, P. Magnoux and J. Mijoin, *Catal. Today*, 2007, **124**, 118–123.
40 V. V. Pushkarev, V. I. Kovalchuk and J. L. d'Itri, *J. Phys. Chem. B*, 2004, **108**, 5341–5348.
41 Z. Wu, M. Li, J. Howe, H. M. Meyer III and S. H. Overbury, *Langmuir*, 2010, **26**, 16595–16606.
42 X. W. Liu, K. B. Zhou, L. Wang, B. Y. Wang and Y. D. Li, *J. Am. Chem. Soc.*, 2009, **131**, 3140–3141.
43 J. Xu, J. Harmer, G. Li, T. Chapman, P. Collier, S. Longworth and S. C. Tsang, *Chem. Commun.*, 2010, **46**, 1887–1889.
44 N. J. Lawrence, J. R. Brewer, L. Wang, T.-S. Wu, J. Wells-Kingsbury, M. M. Ihrig, G. Wang, Y.-L. Soo, W.-N. Mei and C. L. Cheung, *Nano Lett.*, 2011, **11**, 2666–2671.
45 J. Paier, C. Penschke and J. Sauer, *Chem. Rev.*, 2013, **113**, 3949–3985.
46 M. J. Puska and R. M. Nieminen, *Rev. Mod. Phys.*, 1994, **66**, 841–897.
47 S. J. Chang, M. Li, Q. Hua, L. J. Zhang, Y. S. Ma, B. J. Ye and W. X. Huang, *J. Catal.*, 2012, **293**, 195–204.
48 W. Q. Shi, Y. Z. Li, J. T. Hou, H. Q. Lv, X. J. Zhao, P. F. Fang, F. Zheng and S. J. Wang, *J. Mater. Chem. A*, 2013, **1**, 728–734.
49 A. V. Thorat, T. Ghoshal, J. D. P. Holmes, M. G. Nambissanc and M. A. A. Morris, *Nanoscale*, 2014, **6**, 608–615.
50 Y. Zhao, B.-T. Teng, X.-D. Wen, Y. Zhao, Q.-P. Chen, L.-H. Zhao and M.-F. Luo, *J. Phys. Chem. C*, 2012, **116**, 15986–15991.
51 Z. Wu, M. Li and S. H. Overbury, *J. Catal.*, 2012, **285**, 61–73.
52 T. X. T. Sayle, S. C. Parker and C. R. A. Catlow, *Surf. Sci.*, 1994, **316**, 329–336.
53 M. Nolan, S. C. Parker and G. W. Watson, *Surf. Sci.*, 2005, **595**, 223–232.
54 U. M. Bhatta, I. M. Ross, T. X. T. Sayle, D. C. Sayle, S. C. Parker, D. Reid, S. Seal, A. Kumar and G. Möbus, *ACS Nano*, 2012, **6**, 421–430.
55 Y. Lin, Z. Wu, J. Wen, K. R. Poeppelmeier and L. D. Marks, *Nano Lett.*, 2014, **14**, 191–196.
56 T. Mitsui, M. K. Rose, E. Fomin, D. F. Ogletree and M. Salmeron, *Nature*, 2003, **422**, 705–707.
57 D. E. Jiang and S. Dai, *Phys. Chem. Chem. Phys.*, 2011, **13**, 978–984.

58 Y. B. Yu, J. J. Zhao, X. Han, Y. Zhang, X. B. Qin and B. Y. Wang, *Cuihua Xuebao*, 2013, **34**, 283–293.
59 Y. B. Yu, T. Takei, H. Ohashi, H. He, X. L. Zhang and M. Haruta, *J. Catal.*, 2009, **267**, 121–128.
60 D. C. Sayle, X. D. Feng, Y. Ding, Z. L. Wang and T. X. T. Sayle, *J. Am. Chem. Soc.*, 2007, **129**, 7924–7935.
61 T. X. T. Sayle, M. Cantoni, U. M. Bhatta, S. C. Parker, S. R. Hall, G. Möbus, M. Molinari, D. Reid, S. Seal and D. C. Sayle, *Chem. Mater.*, 2012, **24**, 1811–1821.
62 A. Migani, G. N. Vayssilov, S. T. Bromley, F. Illas and K. M. Neyman, *J. Mater. Chem.*, 2010, **20**, 10535–10546.
63 N. Nilius, S. M. Kozlov, J.-F. Jerratsch, M. Baron, X. Shao, F. Viñes, S. Shaikhutdinov, K. M. Neyman and H.-J. Freund, *ACS Nano*, 2012, **6**, 1126–1133.
64 T. H. de Keijser, J. I. Langford, E. J. Mittemeijer and A. B. P. Vogels, *J. Appl. Crystallogr.*, 1982, **15**, 308–314.
65 R. Si and M. Flytzani-Stephanopoulos, *Angew. Chem., Int. Ed.*, 2008, **47**, 2884–2887.
66 B. Murugan and A. V. Ramaswamy, *J. Am. Chem. Soc.*, 2007, **129**, 3062–3063.
67 N. E. Ntainjua, T. Garcia, B. Solsona and S. H. Taylor, *Catal. Today*, 2008, **137**, 373–378.
68 M. B. Watkins, A. S. Foster and A. L. Shluger, *J. Phys. Chem. C*, 2007, **111**, 15337–15341.
69 M. Molinari, S. C. Parker, D. C. Sayle and M. S. Islam, *J. Phys. Chem. C*, 2012, **116**, 7073–7082.
70 C. Padeste, N. W. Cant and D. L. Trimm, *Catal. Lett.*, 1993, **18**, 305–316.

